A three-dimensional phase field model for nanowire growth by the vapor–liquid–solid mechanism

2014 Modelling Simul. Mater. Sci. Eng. 22 055005

(http://iopscience.iop.org/0965-0393/22/5/055005)

IOP Publishing
Modelling and Simulation in Materials Science and Engineering

Modelling Simul. Mater. Sci. Eng. **22** (2014) 055005 (15pp)
doi:10.1088/0965-0393/22/5/055005

A three-dimensional phase field model for nanowire growth by the vapor–liquid–solid mechanism

Yanming Wang[1], **Seunghwa Ryu**[2], **Paul C McIntyre**[1] **and Wei Cai**[1,3]

[1] Department of Materials Science and Engineering, Stanford University, Stanford, CA, USA
[2] Department of Mechanical Engineering, Korea Advanced Institute of Science and Technology, Yuseong-gu, Daejeon, Korea 305-701
[3] Department of Mechanical Engineering, Stanford University, Stanford, CA 94305, USA

E-mail: caiwei@stanford.edu

Received 16 February 2014
Accepted for publication 27 February 2014
Published 15 May 2014

Abstract

We present a three-dimensional multi-phase field model for catalyzed nanowire (NW) growth by the vapor–liquid–solid (VLS) mechanism. The equation of motion contains both a Ginzburg–Landau term for deposition and a diffusion (Cahn–Hilliard) term for interface relaxation without deposition. Direct deposition from vapor to solid, which competes with NW crystal growth through the molten catalyst droplet, is suppressed by assigning a very small kinetic coefficient at the solid–vapor interface. The thermodynamic self-consistency of the model is demonstrated by its ability to reproduce the equilibrium contact angles at the VLS junction. The incorporation of orientation dependent gradient energy leads to faceting of the solid–liquid and solid–vapor interfaces. The model successfully captures the curved shape of the NW base and the Gibbs–Thomson effect on growth velocity.

Keywords: multi-phase field model, vapor–liquid–solid growth, three dimensional, nanowire

(Some figures may appear in colour only in the online journal)

S Online supplementary data available from stacks.iop.org/MSMSE/22/055005/mmedia

0965-0393/14/055005+15$33.00

1. Introduction

Nanowires (NWs) show promise in many new application areas such as integrated circuits, solar cells, batteries and biosensors [1, 2]. The catalyzed growth of NWs by the vapor–liquid–solid (VLS) mechanism is a widely used method for NW fabrication. Yet there are still many fundamental questions about the VLS mechanism that are not well understood. For example, it is not clear why a certain fraction of catalyst nanoparticles fails to nucleate NWs, or what causes growth anomalies such as kinking during steady state NW growth. Finding answers to such fundamental questions is critical to achieve better control over NW orientation, yield and quality, which is necessary for incorporating lab-grown NWs into real-world applications.

Experimental characterization techniques have revealed important information about the VLS mechanism [3–8]. However, experimental methods still face fundamental limits in terms of spatial and temporal resolution, and can be complemented by theoretical and computational models. Many simulation techniques have been applied to study the VLS growth mechanism. Molecular dynamics (MD) simulation provides full atomistic details of the VLS growth process [9, 10], but its time scale is very limited and many orders of magnitude smaller than experimental time scales. On the other hand, continuum models can usually access much larger time (and length) scales that overlap with experiments. Generally speaking, there are two continuum approaches to model morphology changes: the front-tracking method and the phase field method [11]. The front-tracking method is usually computationally more efficient, but the phase field method is usually easier to implement, especially when three-dimensional (3D). Both the front-tracking model [12] and the phase field model [13, 14] have been developed for two-dimensional (2D) VLS growth. However certain features of the NWs cannot be properly represented in two dimensions, such as the facets of NW sidewall and the shape of NW cross section. Therefore, there is a pressing need for a continuum model for 3D VLS growth.

In this paper, we present a 3D multi-phase field model of VLS growth that can access the experimental length and time scale. The rest of this paper is organized as follows. Section 2 presents the multi-phase field model, including the free energy functional, equation of motion and method of integration. Section 3 provides the energetic and kinetic parameters for the model and describes how they are chosen. Section 4 presents simulation results, including the equilibrium structure of the VLS junction, and the non-equilibrium process of NW growth. A brief summary is given in section 5.

2. Multi-phase field formulation of VLS growth

2.1. Degrees of freedom

We adopt the multi-phase field formulation of Folch and Plapp [15] and Steinbach and Pezzolla [16]. The fundamental degrees of freedom in our model are three phase fields: $\phi_{\mathrm{L}}(\boldsymbol{x})$, $\phi_{\mathrm{S}}(\boldsymbol{x})$ and $\phi_{\mathrm{V}}(\boldsymbol{x})$, representing the liquid, solid and vapor phase, respectively. For example, $\phi_{\mathrm{L}}(\boldsymbol{x}) = 1$ means point $\boldsymbol{x}$ is in the liquid phase and $\phi_{\mathrm{L}}(\boldsymbol{x}) = 0$ means point $\boldsymbol{x}$ is not in the liquid phase. The region where $\phi_{\mathrm{L}}(\boldsymbol{x})$ changes from 0 to 1 is the boundary between the liquid and the other phases. Because every point in the simulation domain must be in one of the three phases (or their boundaries), the three phase fields are subjected to the following constraint at every point $\boldsymbol{x}$:

$$\phi_{\mathrm{L}}(\boldsymbol{x}) + \phi_{\mathrm{S}}(\boldsymbol{x}) + \phi_{\mathrm{V}}(\boldsymbol{x}) = 1. \tag{1}$$

2.2. Free energy functional

The total free energy of the system is a functional of the three phase fields and consists of separate contributions from the three phases [15],

$$\begin{aligned} F[\phi_{\mathrm{L}}(\boldsymbol{x}), \phi_{\mathrm{S}}(\boldsymbol{x}), \phi_{\mathrm{V}}(\boldsymbol{x})] = & \sum_{i=\mathrm{S,L,V}} \int f_i(\phi_i(\boldsymbol{x}), \nabla\phi_i(\boldsymbol{x}))\,\mathrm{d}^3\boldsymbol{x} \\ & + \int P\,\phi_{\mathrm{V}}^2(\boldsymbol{x})\,\phi_{\mathrm{L}}^2(\boldsymbol{x})\,\phi_{\mathrm{S}}^2(\boldsymbol{x})\,\mathrm{d}^3\boldsymbol{x} \end{aligned} \tag{2}$$

where f_i is the local free energy density of phase i,

$$f_i(\phi_i, \nabla\phi_i) = U_i\phi_i^2(1-\phi_i^2) + \epsilon_i^2\,|\nabla\phi_i|^2 + \mu_i\,\rho_0\,C(\phi_i). \tag{3}$$

The local free energy density, as given in equation (3), has three parts. The first term, $U_i\phi_i^2(1-\phi_i^2)$, is a double well function to penalize any deviation of ϕ_i from 0 or 1. This term stabilizes the phases and can be considered as the free energy density of the bulk. The second term, $\epsilon_i^2|\nabla\phi_i|^2$, penalizes variation of the phase field in space and gives rise to positive interface energies. To capture the anisotropy of the solid surface (i.e. when $i = \mathrm{S}$), ϵ_{S} is a function of the local orientation $\boldsymbol{n}_{\mathrm{S}}$ of the surface normal, where

$$\boldsymbol{n}_{\mathrm{S}} = \frac{\nabla\phi_{\mathrm{S}}}{|\nabla\phi_{\mathrm{S}}|}. \tag{4}$$

The function $\epsilon_{\mathrm{S}}(\boldsymbol{n})$ is constructed to satisfy cubic symmetry [13, 17]:

$$\begin{aligned} \epsilon_{\mathrm{S}}(\boldsymbol{n}) = \epsilon_{\mathrm{S}0}\cdot\big[1 &+ e_{\mathrm{S}1}\cdot(n_x^2n_y^2 + n_y^2n_z^2 + n_z^2n_x^2) + e_{\mathrm{S}2}\cdot(n_x^2n_y^2n_z^2) \\ &+ e_{\mathrm{S}3}\cdot(n_x^2n_y^2 + n_y^2n_z^2 + n_z^2n_x^2)^2\big], \end{aligned} \tag{5}$$

where $\epsilon_{\mathrm{S}0}$, $e_{\mathrm{S}1}$, $e_{\mathrm{S}2}$ and $e_{\mathrm{S}3}$ are constants chosen to reproduce the experimental data on interface energies of various facets (see section 3). For liquid and vapor phases, ϵ_{L} and ϵ_{V} are constants. The third term in the local free energy density, $\mu_i\,\rho_0\,C(\phi_i)$, accounts for the effect from the chemical potential difference between the phases (which provides the driving force for NW growth). μ_i is the chemical potential of Si (or Ge) in phase i, and ρ_0 is the material's atomic density in the liquid or the solid phase (taken to be a constant here for simplicity[4]). In this work, we take $\rho_0 = (a_0^3/8)^{-1}$, where a_0 is the lattice constant of Si or Ge. Consequently,

$$\Omega_i \equiv \int C(\phi_i)\,\mathrm{d}^3\boldsymbol{x} \tag{6}$$

can be interpreted as the volume occupied by phase i. In this work, we use the following definition:

$$C(\phi_i) = [\tanh(10\,\phi_i - 5) + 1]\,/2. \tag{7}$$

The advantage of this choice is that it produces a zero derivative at $\phi_i = 0$ and 1 [15], which prevents the shift of the minimum of the ϕ_i values in the bulk region away from 0 and 1, when the chemical potentials of the three phases are not the same.

The second term in equation (2) penalizes the co-existence of three phases at the same point. It is zero in pure phase regions ($\phi_i(\boldsymbol{x}) = 1$), as well as in two-phase interfaces ($\phi_i(\boldsymbol{x}) + \phi_j(\boldsymbol{x}) = 1$). Without this term, the third phase (e.g. liquid) is often found to be trapped at a two-phase (e.g. solid–vapor) interface, which is unphysical. This term is added to make it energetically unfavorable for the third phase to co-exist at the two-phase interface.

---

[4] The vapor phase obviously has a much smaller density than the liquid and solid phases. However, under experimental conditions, the vapor phase is connected to a reservoir much greater than the simulation cell, so that it is an acceptable approximation to ignore the density difference between all phases in the phase field simulation.

This penalty function is likely to modify the line tension of triple-junction. In section 4, we will show that this term has negligible effect on the equilibrium contact angle at the triple-junction, when the junction line is perfectly straight. The effect of this penalty function on the line tension of the triple-junction will be investigated in the future.

2.3. Equation of motion

The equation of motion in our phase field model is

$$\frac{\mathrm{d}\phi_i(t)}{\mathrm{d}t} = G_i^{\mathrm{GL}}[\{\phi_j(t)\}] + G_i^{\mathrm{D}}[\{\phi_j(t)\}] \tag{8}$$

$$\begin{aligned} G_i^{\mathrm{GL}}[\{\phi_j(t)\}] = &-\Gamma_{im}(\boldsymbol{x})\left\{K_{im}^{\mathrm{GL}}\left(\frac{\delta F}{\delta\phi_i}-\frac{\delta F}{\delta\phi_m}\right)+K_0^{\mathrm{GL}}\left[\frac{1}{2}\left(\frac{\delta F}{\delta\phi_i}+\frac{\delta F}{\delta\phi_m}\right)-\frac{\delta F}{\delta\phi_n}\right]\right\} \\ &-\Gamma_{in}(\boldsymbol{x})\left\{K_{in}^{\mathrm{GL}}\left(\frac{\delta F}{\delta\phi_i}-\frac{\delta F}{\delta\phi_n}\right)+K_0^{\mathrm{GL}}\left[\frac{1}{2}\left(\frac{\delta F}{\delta\phi_i}+\frac{\delta F}{\delta\phi_n}\right)-\frac{\delta F}{\delta\phi_m}\right]\right\} \\ &-[1-\Gamma_{im}(\boldsymbol{x})-\Gamma_{in}(\boldsymbol{x})]\;K_0^{\mathrm{GL}}\left[2\frac{\delta F}{\delta\phi_i}-\left(\frac{\delta F}{\delta\phi_m}+\frac{\delta F}{\delta\phi_n}\right)\right] \end{aligned} \tag{9}$$

$$G_i^{\mathrm{D}}[\{\phi_j(t)\}] = K^{\mathrm{D}}\nabla^2\left[2\frac{\delta F}{\delta\phi_i}-\left(\frac{\delta F}{\delta\phi_m}+\frac{\delta F}{\delta\phi_n}\right)\right], \tag{10}$$

$$\text{where } i, j, m, n = \mathrm{S}, \mathrm{V}, \mathrm{L} \quad \text{and } m \neq i,\; n \neq i,\; m \neq n$$

subjected to the constraint

$$\Omega_{\mathrm{L}} = \text{constant} \tag{11}$$

as well as the constraint given by equation (1). $G_i^{\mathrm{GL}}[\cdot]$ and $G_i^{\mathrm{D}}[\cdot]$ are time-derivative contributions in the form of the Ginzburg–Landau (GL) and diffusion (i.e. Cahn–Hilliard), respectively. For clarity, we write out the case for $i = \mathrm{L}$ (liquid phase) explicitly.

$$\begin{aligned} G_{\mathrm{L}}^{\mathrm{GL}}[\{\phi_j(t)\}] = &-\Gamma_{\mathrm{LV}}(\boldsymbol{x})\left\{K_{\mathrm{LV}}^{\mathrm{GL}}\left(\frac{\delta F}{\delta\phi_{\mathrm{L}}}-\frac{\delta F}{\delta\phi_{\mathrm{V}}}\right)+K_0^{\mathrm{GL}}\left[\frac{1}{2}\left(\frac{\delta F}{\delta\phi_{\mathrm{L}}}+\frac{\delta F}{\delta\phi_{\mathrm{V}}}\right)-\frac{\delta F}{\delta\phi_{\mathrm{S}}}\right]\right\} \\ &-\Gamma_{\mathrm{LS}}(\boldsymbol{x})\left\{K_{\mathrm{LS}}^{\mathrm{GL}}\left(\frac{\delta F}{\delta\phi_{\mathrm{L}}}-\frac{\delta F}{\delta\phi_{\mathrm{S}}}\right)+K_0^{\mathrm{GL}}\left[\frac{1}{2}\left(\frac{\delta F}{\delta\phi_{\mathrm{L}}}+\frac{\delta F}{\delta\phi_{\mathrm{S}}}\right)-\frac{\delta F}{\delta\phi_{\mathrm{V}}}\right]\right\} \\ &-[1-\Gamma_{\mathrm{LV}}(\boldsymbol{x})-\Gamma_{\mathrm{LS}}(\boldsymbol{x})]\;K_0^{\mathrm{GL}}\left[2\frac{\delta F}{\delta\phi_{\mathrm{L}}}-\left(\frac{\delta F}{\delta\phi_{\mathrm{V}}}+\frac{\delta F}{\delta\phi_{\mathrm{S}}}\right)\right] \end{aligned} \tag{12}$$

$$G_{\mathrm{L}}^{\mathrm{D}}[\{\phi_j(t)\}] \;= K^{\mathrm{D}}\nabla^2\left[2\frac{\delta F}{\delta\phi_{\mathrm{L}}}-\left(\frac{\delta F}{\delta\phi_{\mathrm{V}}}+\frac{\delta F}{\delta\phi_{\mathrm{S}}}\right)\right]. \tag{13}$$

Note that the GL term by itself does not conserve the volume Ω_i of any of the three phases. This term is needed to model NW growth during which Ω_{S} grows at the expense of Ω_{V}. In contrast, $G_i^{\mathrm{D}}[\cdot]$, which can be derived from a conservation law that is similar to the Fick's law, describes the diffusion process of the phase fields. Consequently, it does not modify the volume of any phases, and helps to adjust the shape of the interface to lower the free energy[5]. The diffusion term can lead to faceting of the solid surface, e.g. the NW side wall, even in the absence of side-wall deposition.

The constraint on the total liquid volume, equation (11), is an approximation based on the fact that the volume of the liquid alloy catalyst often does not change appreciably during

---

[5] To be more precise, the diffusion term only conserves $\hat{\Omega}_i \equiv \int \phi_i \,\mathrm{d}^3\boldsymbol{x}$, which is not exactly the same as Ω_i defined in equation (6). However, $\hat{\Omega}_i$ is close to Ω_i so that the diffusion term does not disturb the conservation of Ω_i appreciably.

NW growth, after the catalyst has melted. Without this constraint, a simulation based on equation (8) would quickly see the liquid volume vanish, which is clearly unphysical. A more refined model would be to make Ω_L depend on the temperature, vapor pressure and possible loss of catalyst through diffusion; but that model is beyond the scope of this paper. Because of the constraint on liquid volume, only two chemical potentials, μ_V and μ_S, can be specified as input parameters, while μ_L is automatically adjusted to satisfy equation (11). The resulting μ_L is usually between μ_V and μ_S during the simulation. The implementation of this constraint will be discussed in section 2.4.

Functions $\Gamma_{im}(\boldsymbol{x}) = \Gamma_{mi}(\boldsymbol{x})$ are designed to indicate the regions around the interface between phase i and phase m. Their values are either 0 or 1 at every point $\boldsymbol{x}$. For example, if $\Gamma_\mathrm{SL}(\boldsymbol{x}) = 1$, then $\boldsymbol{x}$ is close to the solid–liquid interface. The algorithm we use to determine the values of $\Gamma_{im}(\boldsymbol{x})$ will be described in section 2.5.

Equation (9) shows that the driving force for the growth (or shrinkage) of phase i is provided by the differences between the variational derivatives with respect to phase i and other phases. For example, at the i–m interface, the driving force for phase transition from ϕ_m to ϕ_i is provided by $\frac{\delta F}{\delta\phi_i} - \frac{\delta F}{\delta\phi_m}$. The kinetic coefficient for this phase transition is K^GL_{im}. These explain the first term in the bracket of the first line of equation (9).

At the i–m interface, phase n would be the 'third phase'. We allow the third phase to flow out of the interface, driven by the penalty function $P\phi_\mathrm{V}^2\phi_\mathrm{L}^2\phi_\mathrm{S}^2$ in equation (3). We do not want the i–m interface to move as phase n flows out of the interface. In other words, equal amount of phase i and phase m should be converted from phase n in this process. Hence, the driving force for this process is $\frac{1}{2}(\frac{\delta F}{\delta\phi_i} + \frac{\delta F}{\delta\phi_m}) - \frac{\delta F}{\delta\phi_n}$. The kinetic coefficient for this process is designated as K^GL_0. This explains the second term in the bracket of the first line of equation (9). It can be verified that the equation of motion given in the above satisfies the constraint, $\frac{\mathrm{d}\phi_\mathrm{V}(t)}{\mathrm{d}t} + \frac{\mathrm{d}\phi_\mathrm{L}(t)}{\mathrm{d}t} + \frac{\mathrm{d}\phi_\mathrm{S}(t)}{\mathrm{d}t} = 0$ at every point $\boldsymbol{x}$, which is required by equation (1).

For simplicity, we set $K^\mathrm{GL}_\mathrm{LV} = K^\mathrm{GL}_\mathrm{LS} = K^\mathrm{GL}_0$ in this work. However, we set $K^\mathrm{GL}_\mathrm{SV}$ to be much smaller than K^GL_0. This is to capture the effect that the direct deposition rate at the vapor–solid interface is much smaller than that at the vapor–liquid and liquid–solid interface during NW growth by the VLS mechanism. This is not due to a lack of driving force, but is due to a much smaller kinetic coefficient (i.e. lack of catalyst).

Given that the local free energy density depends on the local values of ϕ_i and the local gradient $\nabla\phi_i$, the variational derivative of F has the following form:

$$\frac{\delta F}{\delta\phi_i} = \frac{\partial f_i}{\partial\phi_i} - \nabla\left[\frac{\partial f_i}{\partial(\nabla\phi_i)}\right] + \frac{\partial}{\partial\phi_i}\left(P\phi_\mathrm{V}^2\phi_\mathrm{L}^2\phi_\mathrm{S}^2\right) \tag{14}$$

$$\begin{aligned} &= U_i\left(4\phi_i^3 - 6\phi_i^2 + 2\phi_i^2\right) + \mu_i\,\rho_0\,C'(\phi_i) + \frac{\partial}{\partial\phi_i}\left(P\phi_\mathrm{V}^2\phi_\mathrm{L}^2\phi_\mathrm{S}^2\right) - \nabla\cdot\left[(\epsilon_i(\boldsymbol{n}_i))^2\nabla\phi_i\right] \\ &\quad - \sum_{j=1,2,3}\frac{\partial}{\partial x_j}\left[(\nabla\phi_i)^2\epsilon_i(\boldsymbol{n}_i)\frac{\partial\epsilon_i(\boldsymbol{n}_i)}{\partial\phi_{i,j}}\right], \end{aligned} \tag{15}$$

$x_1 \equiv x, x_2 \equiv y, x_3 \equiv z$ and $\phi_{i,j} \equiv \partial\phi_i/\partial x_j$. The last term in equation (15) is non-zero only for $i = \mathrm{S}$. Given the choice made in equation (7), $C'(\phi_i) = 5 - 5\tanh^2(10\phi_i - 5)$.

2.4. Constraint on liquid volume

Since the $G^\mathrm{D}[\cdot]$ automatically conserves the individual volumes of all three phases, the constraint on Ω_L only influences the implementation of $G^\mathrm{GL}[\cdot]$. Hence we will ignore $G^\mathrm{D}[\cdot]$ for the rest of this section. Taking the time derivative on both sides of equation (11), we get

$$0 = \frac{\mathrm{d}\Omega_\mathrm{L}}{\mathrm{d}t} = \int C'(\phi_\mathrm{L})\cdot G^\mathrm{GL}_\mathrm{L}(\{\phi_j\};\mu_\mathrm{L})\,\mathrm{d}^3\boldsymbol{x}, \tag{16}$$

where for clarity the dependence of $G_{\mathrm{L}}^{\mathrm{GL}}$ on μ_{L} is written out explicitly. Therefore, the goal is to find μ_{L} that satisfies equation (16). Because $G_{\mathrm{L}}^{\mathrm{GL}}$ has a linear dependence on μ_{L}, equation (16) can be solved by a predictor-corrector approach. First, we assume the liquid chemical potential is an arbitrary constant (predictor), μ_{L}^* (e.g. we can choose $\mu_{\mathrm{L}}^* = \mu_{\mathrm{S}}$). The trial time derivative $G_{\mathrm{L}}^{\mathrm{GL}}(\{\phi_j\};\, \mu_{\mathrm{L}}^*)$ is evaluated. The true time derivative, $G_{\mathrm{L}}^{\mathrm{GL}}(\{\phi_j\};\, \mu_{\mathrm{L}})$, corresponding to the still unknown μ_{L}, can be written as

$$G_{\mathrm{L}}^{\mathrm{GL}}(\{\phi_j\};\, \mu_{\mathrm{L}}) = G_{\mathrm{L}}^{\mathrm{GL}}(\{\phi_j\};\, \mu_{\mathrm{L}}^*) + \Delta\mu_{\mathrm{L}}\, g_{\mu_{\mathrm{L}}}(\boldsymbol{x}), \tag{17}$$

where

$$\Delta\mu_{\mathrm{L}} \equiv \mu_{\mathrm{L}} - \mu_{\mathrm{L}}^* \tag{18}$$

$$\begin{aligned} g_{\mu_{\mathrm{L}}}(\boldsymbol{x}) \equiv {} & \frac{\partial}{\partial \mu_{\mathrm{L}}}\left[G_{\mathrm{L}}^{\mathrm{GL}}(\{\phi_j\};\, \mu_{\mathrm{L}})\right] \\ = {} & -\Gamma_{\mathrm{LV}}(\boldsymbol{x})\left(K_{\mathrm{LV}}^{\mathrm{GL}} + \frac{1}{2}K_0^{\mathrm{GL}}\right)\rho_0 C'(\phi_{\mathrm{L}}) - \Gamma_{\mathrm{LS}}(\boldsymbol{x})\left(K_{\mathrm{LS}}^{\mathrm{GL}} + \frac{1}{2}K_0^{\mathrm{GL}}\right)\rho_0 C'(\phi_{\mathrm{L}}) \\ & -2\,[1 - \Gamma_{\mathrm{LV}}(\boldsymbol{x}) - \Gamma_{\mathrm{LS}}(\boldsymbol{x})]\, K_0^{\mathrm{GL}}\, \rho_0 C'(\phi_{\mathrm{L}}). \end{aligned} \tag{19}$$

In the special case of $K_{\mathrm{LV}}^{\mathrm{GL}} = K_{\mathrm{LS}}^{\mathrm{GL}} = K_0^{\mathrm{GL}}$, we have

$$g_{\mu_{\mathrm{L}}}(\boldsymbol{x}) = -\left\{\frac{3}{2}\,\Gamma_{\mathrm{LV}}(\boldsymbol{x}) + \frac{3}{2}\,\Gamma_{\mathrm{LS}}(\boldsymbol{x}) + 2\,[1 - \Gamma_{\mathrm{LV}}(\boldsymbol{x}) - \Gamma_{\mathrm{LS}}(\boldsymbol{x})]\right\} K_0^{\mathrm{GL}}\, \rho_0 C'(\phi_{\mathrm{L}}). \tag{20}$$

Given equations (16) and (17), we have

$$0 = \int C'(\phi_{\mathrm{L}}) \cdot \left[G_{\mathrm{L}}^{\mathrm{GL}}(\{\phi_j\};\, \mu_{\mathrm{L}}^*) + \Delta\mu_{\mathrm{L}} g_{\mu_{\mathrm{L}}}(\boldsymbol{x})\right] \mathrm{d}^3\boldsymbol{x}. \tag{21}$$

Therefore, the change of liquid chemical potential (corrector) is

$$\Delta\mu_{\mathrm{L}} = -\frac{\int C'(\phi_{\mathrm{L}}) \cdot G_{\mathrm{L}}^{\mathrm{GL}}(\{\phi_j\};\, \mu_{\mathrm{L}}^*)\, \mathrm{d}^3\boldsymbol{x}}{\int C'(\phi_{\mathrm{L}}) \cdot g_{\mu_{\mathrm{L}}}(\boldsymbol{x})\, \mathrm{d}^3\boldsymbol{x}}. \tag{22}$$

After finding $\Delta\mu_{\mathrm{L}}$, the true time derivative can be obtained by equation (17).

2.5. Interface identification

Given the phase fields $\{\phi_i(\boldsymbol{x})\}$, we need to identify the functions $\Gamma_{\mathrm{LS}}(\boldsymbol{x})$, $\Gamma_{\mathrm{LV}}(\boldsymbol{x})$ and $\Gamma_{\mathrm{SV}}(\boldsymbol{x})$ that describe the regions occupied by the solid–liquid, liquid–vapor and solid–vapor interfaces, respectively.

In this work, we represent the phase fields on a uniform 3D grid $\{\boldsymbol{x}_n\}$, where $\boldsymbol{n}$ represents three integer indices to uniquely specify a grid point. We introduce the following definition at every grid point $\boldsymbol{x}_n$:

$$b_i(\boldsymbol{x}_n) \equiv \min_{|\boldsymbol{x}_m - \boldsymbol{x}_n| \leqslant r_c} \{[\phi_i(\boldsymbol{x}_n) - 0.5] \cdot [\phi_i(\boldsymbol{x}_m) - 0.5]\}. \tag{23}$$

The minimization is taken over all grid points $\boldsymbol{x}_m$ within a cut-off radius r_c of $\boldsymbol{x}_n$, which depends on the interface thickness. Because the boundary of phase i can be related to the isosurface of $\phi_i(\boldsymbol{x}) = 0.5$, we define that $\boldsymbol{x}_n$ belongs to the boundary Γ_i of phase i if and only if $b_i(\boldsymbol{x}_n) < 0$, i.e.

$$\Gamma_i(\boldsymbol{x}_n) = \begin{cases} 1 & \text{if} \quad b_i(\boldsymbol{x}_n) < 0 \\ 0 & \text{if} \quad b_i(\boldsymbol{x}_n) \geqslant 0. \end{cases} \tag{24}$$

Given the functions $\Gamma_{\mathrm{S}}(\boldsymbol{x})$ and $\Gamma_{\mathrm{L}}(\boldsymbol{x})$ that describes the solid and liquid surface regions, the two-phase interface regions are defined as follows:

$$\Gamma_{\mathrm{LS}}(\boldsymbol{x}) = \Gamma_{\mathrm{S}}(\boldsymbol{x})\, \Gamma_{\mathrm{L}}(\boldsymbol{x}) \tag{25}$$

$$\Gamma_{\mathrm{SV}}(\boldsymbol{x}) = \Gamma_{\mathrm{S}}(\boldsymbol{x})\, [1 - \Gamma_{\mathrm{L}}(\boldsymbol{x})] \tag{26}$$

$$\Gamma_{\mathrm{LV}}(\boldsymbol{x}) = [1 - \Gamma_{\mathrm{S}}(\boldsymbol{x})]\, \Gamma_{\mathrm{L}}(\boldsymbol{x}). \tag{27}$$

Table 1. Experimental data on interface energy in J/m^2. The solid phase is the semiconductor, i.e. Si or Ge. The liquid phase is the Si–Au or Ge–Au binary alloy near eutectic point. The solid–vapor interface energy depends on the orientation because of anisotropy.

Material	$\sigma_{\rm LS}$	$\sigma_{\rm LV}$	$\sigma_{\rm SV(111)}$	$\sigma_{\rm SV(100)}$	$\sigma_{\rm SV(311)}$	$\sigma_{\rm SV(110)}$
Si & Au	0.62 [3]	0.85 [18]	1.24 [19]	1.36 [20]	1.38 [20]	1.43 [20]
Ge & Au	0.55 [21]	0.94 [18]	1.06 [19]			

2.6. Integrator

For simplicity, we use the Euler forward integrator to compute the phase field values at the next time step $t + \Delta t$ based on the values at time t,

$$\phi_i(t+\Delta t) = \phi_i(t) + G_i^{\rm GL}[\{\phi_j(t)\}]\,\Delta t + G^{\rm D}[\{\phi_j(t)\}]\,\Delta t. \tag{28}$$

However, the step size Δt is not a constant. Instead, it is capped at a maximum value, $\Delta t_{\rm max}$, and is also constrained to limit the maximum change of phase fields in one simulation step to within $\Delta\phi_{\rm max}$. Therefore, at each time step, Δt is specified by

$$\Delta t = \min\left[\min_{i,\boldsymbol{x}}\left(\frac{\left|G_i^{\rm GL}[\{\phi_j(\boldsymbol{x},t)\}] + G_i^{\rm D}[\{\phi_j(\boldsymbol{x},t)\}]\right|}{\Delta\phi_{\rm max}}\right), \Delta t_{\rm max}\right]. \tag{29}$$

The resulting time step is usually smaller at the beginning of the simulation, due to certain unphysical features (e.g. abrupt changes in the phase field values) in the initial configuration. The time step becomes larger as these unphysical features disappear during the simulation.

3. Model parameters

In this section, we describe the choices of parameters in our phase field model, including the unit system and the relationship between different parameters. We adopt the convention that the unit of energy is eV; the unit of length is Å; and the unit of time is s (second). The energy parameters, such as U_i and ϵ_i, in the model are determined by the interface energy σ and the interface thickness ξ. In Folch and Plapp's formulation [15], which is adopted here, the equilibrium solution of a planar interface between phases i and j with a normal vector $\boldsymbol{n}$ has the following form:

$$\phi_i(\boldsymbol{x}) = \frac{1}{2}\left[1 + \tanh(\boldsymbol{x}\cdot\boldsymbol{n}/\xi)\right] \tag{30}$$

$$\phi_j(\boldsymbol{x}) = \frac{1}{2}\left[1 - \tanh(\boldsymbol{x}\cdot\boldsymbol{n}/\xi)\right]. \tag{31}$$

The free energy (per unit area) and thickness of this interface are given by

$$\sigma_{ij} = \frac{1}{3}\sqrt{(U_i + U_j)\cdot\left[\epsilon_i^2(\boldsymbol{n}) + \epsilon_j^2(\boldsymbol{n})\right]} \tag{32}$$

$$\xi_{ij} = 2\sqrt{\frac{\epsilon_i^2(\boldsymbol{n}) + \epsilon_j^2(\boldsymbol{n})}{U_i + U_j}}. \tag{33}$$

Table 1 lists the experimental data on the various interface energies in the Si–Au and Ge–Au binary systems. The phase field parameters are chosen to reproduce these interface energies. However, for computational efficiency, the interface thickness in phase field models

Table 2. Parameters in the phase field model. Both ϵ_i^2/ξ and $U_i\,\xi$ are in units of eV/Å^2. ρ_0 is in units of Å^{-3}. P is in units of eV/Å^3. $K_{\rm SV}^{\rm GL}$, $K_0^{\rm GL}$are in units of Å^3/(eV·s). $K^{\rm D}$ is in units of Å^5/(eV·s).

Material	$\epsilon_{\rm L}^2/\xi$	$\epsilon_{\rm S0}^2/\xi$	$\epsilon_{\rm V}^2/\xi$	$U_{\rm L}\,\xi$	$U_{\rm S}\,\xi$	$U_{\rm V}\,\xi$	ρ_0	P
Si & Au	0.0108	0.0709	0.0689	0.0431	0.1894	0.2756	0.0499	0.5
Ge & Au	0.0202	0.0516	0.0680	0.0806	0.1256	0.2719	0.0442	0.5
Material	$e_{\rm S1}$	$e_{\rm S2}$	$e_{\rm S3}$	$K_{\rm SV}^{\rm GL}$	$K_0^{\rm GL}$	$K^{\rm D}$		
Si & Au	0.7024	−7.5943	−1.2231	100/3	$10^5/3$	500/3		
Ge & Au	0.8359	−8.9749	−1.4927	100/3	$10^5/3$	500/3		

is usually much larger than the thickness of real interfaces (often only a few Å's). For simplicity, we choose a common thickness ξ for liquid–vapor, liquid–solid (1 1 1) and vapor–solid (1 1 1) interfaces, i.e.

$$\xi_{\rm LV} = \xi_{\rm LS(111)} = \xi_{\rm SV(111)} = \xi. \tag{34}$$

Given a choice of ξ, the energetic parameters can be obtained from table 2. Due to the lack of experimental data, we assume that the equilibrium shape of Ge nano-crystals is similar to that of Si nano-crystals [22]. This means that we assume the ratios of surface energies of (1 0 0), (3 1 1), (1 1 0) facets over the surface energy of (1 1 1) facet are the same in Ge and Si. For isotropic simulations, $e_{\rm S1}$, $e_{\rm S2}$ and $e_{\rm S3}$ are all set to 0 corresponding to setting the energies of all solid surfaces to be the same as that of the (1 0 0) surface. The kinetic coefficient $K^{\rm GL}$ is chosen so that the NW growth speed predicted by the simulation (see section 4.4) is of the same order of magnitude as experimentally observed values. For the solid–vapor interface, $K_{\rm SV}^{\rm GL}$, is usually set to be about three orders of magnitude smaller than $K_0^{\rm GL}$ to limit side-wall deposition directly from the vapor phase to the NW.

The choice of interface thickness parameter ξ is largely limited by the available computational resources. Here we give a rough estimate assuming a cubic simulation cell with dimension L, uniformly discretized into $N \times N \times N$ grid points. Let h be the physical distance between two neighboring grid points, so that $L = N\,h$. To simulate the VLS growth of an NW with a steady-state growth diameter D, the simulation cell size L must be sufficiently large to hold the initial catalyst, e.g. $L \geqslant 2.5D$. To make sure the NW has a well defined bulk interior, the interface thickness ξ must be small enough so that $D/\xi \geqslant 6$ (an even larger D/ξ is preferable). At the same time, the interface region needs to be well represented by a sufficient number of grid points, so that $\xi/h \geqslant 5$. Therefore, $L \geqslant 75h$, i.e. $N \geqslant 75$ is necessary for a meaningful simulation. At the same time, a serial implementation of the phase field model (i.e. without using parallel processors) is typically limited to $N \leqslant 500$, i.e. up to $500 \times 500 \times 500$ grid points. Therefore, the value of N is limited within the range of 75–500.

To be specific, let us assume $L = 2.5D$ and $\xi/h = 5$. The requirement of $75 \leqslant N \leqslant 500$ translates to $6 \leqslant D/\xi \leqslant 40$. This means that within a set of phase field simulations using identical parameters (including ξ), we can vary the NW diameter by about a factor of 6. For example, if $\xi = 10$ Å, then the NW diameter D can vary from 60 to 400 Å. Parallel implementation is required to simulate thicker NWs without changing ξ.

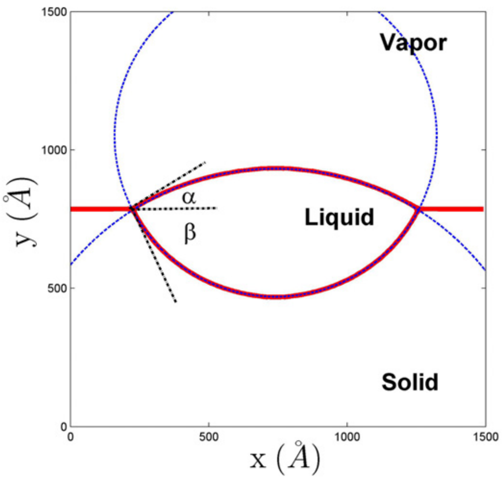

Figure 1. The cross section view of VLS interfaces and the fitting curves for contact angle calculation.

4. Results and discussion

4.1. Young's angle

As a test of the thermodynamic self-consistency of our phase field formulation, we consider a quasi-2D problem where a liquid droplet is equilibrated at the solid–vapor interface, as shown in figure 1. For simplicity, we neglect the anisotropy of the interface energy, i.e. we set $e_{S1} = e_{S2} = e_{S3} = 0$. In this section, we also neglect the interface kinetic coefficient differences and set $K_0^{GL} = K_{SV}^{GL}$. The solid and vapor chemical potential are both set to zero and the liquid volume is constrained to be a constant during the simulation. We define α as the contact angle of the liquid–vapor interface, relative to the solid–vapor interface (which is assumed to be flat). Similarly, we define β as the contact angle of the liquid–solid interface, as shown in figure 1.

At equilibrium, the contact angles α and β are determined by the interface energies through the following equations:

$$\sigma_{SV} = \sigma_{LV} \cos\alpha + \sigma_{LS} \cos\beta \tag{35}$$

$$\sigma_{LV} \sin\alpha = \sigma_{LS} \sin\beta. \tag{36}$$

The contact angles predicted by equations (35) and (36) are given in table 3.

A quasi-2D simulation was conducted with a simulation box size of 1500 Å × 1500 Å. The interface thickness parameter is $\xi = 60$ Å and the grid size is $h = 10$ Å. Periodic boundary conditions are applied in all three directions. The simulation is quasi-2D because for each x and y there is only 1 grid point along the z direction. The initial condition contains a circular liquid droplet with a diameter of 600 Å at the solid–vapor interface. The liquid volume is constrained to be a constant during the simulation (see section 2.4). The simulation is performed for 30 000 steps with $\Delta t_{\max} = 2 \times 10^{-4}$ s and $\Delta\phi_{\max} = 0.005$[6]. The total free energy converges

---

[6] When setting $\Delta t_{\max}$ and $\Delta\phi_{\max}$ values, we consider both the stability and speed of the simulation. Small $\Delta t_{\max}$ and $\Delta\phi_{\max}$ would lower the efficiency of the simulation, while large $\Delta t_{\max}$ and $\Delta\phi_{\max}$ would lead to higher error or even numerical instability. Since the range of ϕ is [0, 1], it is reasonable to limit the phase field change per step to be within 0.5%. The values are determined empirically by trial and error.

Table 3. Young's angle values predicted from force balance equations (35)–(36) compared with those predicted from the phase field simulation, i.e. figure 1.

	From force balance	From simulation
α	31.2°	31.9°
β	62.2°	62.7°

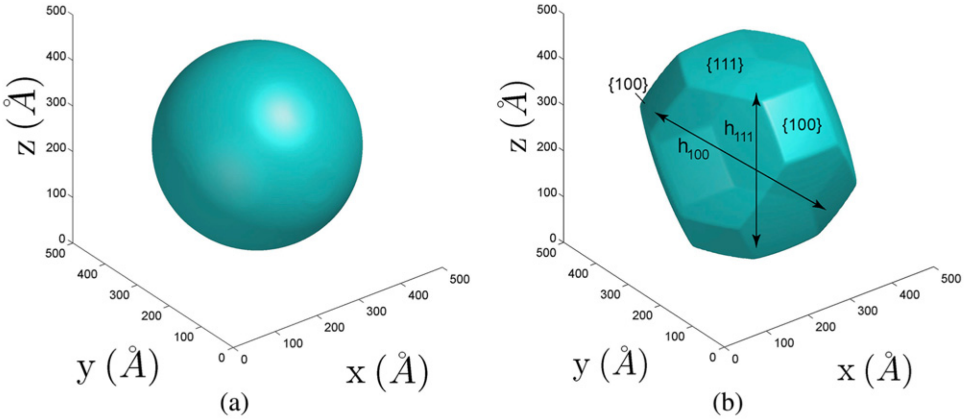

Figure 2. (*a*) The initial condition of a phase field simulation containing a solid sphere surrounded by vapor. (*b*) The snapshot at the end of the simulation, in which the solid phase has evolved to a truncated octahedron.

to a constant value at the end of the simulation, indicating that the equilibrium state has been reached. The shape of the interfaces are identified from the isosurfaces of the ϕ_L at the value 0.5. The part of the isosurface in the region $y \geqslant 800$ Å is attributed to the liquid–vapor interface and the part of the isosurface in the region $y \leqslant 600$ Å is attributed with the liquid–solid interface. The contact angles are extracted by fitting these interface shapes to circular arcs, as shown in figure 1. The results from the fit are listed in table 3. These results are reasonably close to the predictions from force balance equations (within numerical error), validating the thermodynamic self-consistency of our model.

4.2. Equilibrium shape of nano-particle in vapor

In order to test the effect of anisotropy, we performed a simulation with the initial condition containing a solid sphere surrounded by the vapor phase, as shown in figure 2(*a*). The simulation cell size is $500 \times 500 \times 500$ Å^3 and the radius of the solid sphere is 175 Å. The interface thickness parameter is $\xi = 30$ Å and the grid size is $h = 5$ Å. The solid volume is constrained to be a constant in this simulation. The simulation is performed for 10 000 steps with $\Delta t_{\max} = 2 \times 10^{-4}$ s and $\Delta\phi_{\max} = 0.005$. The convergence of the total free energy confirms that the system has reached the equilibrium state at the end of the simulation.

Figure 2(*b*) shows the equilibrium shape of the solid phase, which is similar to a truncated octahedron, consistent with the experimentally observed shape [20] for Si nano-particles. From figure 2(*b*), we can clearly identify two types of facets: the hexagonal shaped $\{1\,1\,1\}$ facet and the square shaped $\{1\,0\,0\}$ facet. This is consistent with table 1, which shows that $\{1\,1\,1\}$ and $\{1\,0\,0\}$ are the two surface orientations with the lowest energies. The distance

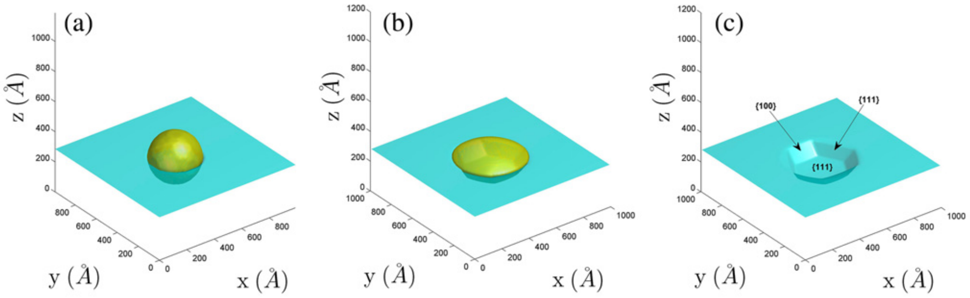

Figure 3. (a) Initial condition of a phase field simulation containing a liquid droplet at the interface between the solid substrate and vapor. (b)–(c) The snapshot at the end of the simulation. Both the liquid and solid surfaces are shown in (b). Only the solid surface is shown in (c) to expose the facets.

between opposing $\{111\}$ facets is $h_{111} = 35.8$ nm, and the distance between opposing $\{1\,0\,0\}$ facets is $h_{1\,1\,1} = 39.1$ nm, as shown in figure 2(b). The ratio $h_{1\,0\,0}/h_{1\,1\,1} \approx 1.1$ agrees with the ratio of the surface energies $\sigma_{1\,0\,0}/\sigma_{1\,1\,1}$ given in table 1. This shows our model is consistent with the Wulff construction [23]. The predicted equilibrium nano-crystal shape is compared with experimental observation [20] in online figure S1 of supplementary materials (stacks.iop.org/MSMSE/22/055005/mmedia).

4.3. Droplet relaxation on substrate

Here we examine the effect of anisotropy on the equilibrium 3D shape of the liquid droplet at the solid–vapor interface. This structure represents the beginning stage of VLS growth, in which the Au catalyst particle has melted into an eutectic liquid alloy, but the gas precursor has not been introduced yet. The simulations are performed using Ge–Au parameters in table 2.

Figure 3(a) shows the initial condition, in which a liquid sphere is placed on a Ge $\langle 1\,1\,1\rangle$ substrate. The simulation cell has dimension $1000 \times 1000 \times 1200\,\text{Å}^3$, with x, y, z axes along $[1\,\bar{1}\,0]$, $[1\,1\,\bar{2}]$ and $[1\,1\,1]$ directions, respectively. The interface thickness parameter is $\xi = 60$ Å and the grid size is $h = 10$ Å. The liquid volume is constrained to be a constant in both the relaxation and NW growth simulations. The solid and vapor phases have the same chemical potential so that the NW does not grow.

The simulation is performed for 10 000 steps with $\Delta t_{\max} = 2\times10^{-4}$ s and $\Delta\phi_{\max} = 0.005$. No visible changes of the interfaces are observed towards the end of the simulation. Figures 3(b) and (c) plots the final, equilibrium shape of the VLS system. Figure 3(b) shows that the liquid–vapor interface remains non-faceted, because its energy is isotropic. Figure 3(c) shows that the liquid–solid interface consists of a large $\{1\,1\,1\}$ facet at the bottom, connected with several smaller $\{1\,1\,1\}$ and $\{1\,0\,0\}$ facets on the side. The VLS junction line has the shape of a (non-regular) hexagon. The faceted shape of the substrate, as etched by the liquid droplet, is compared with TEM observations in online figure S2 of supplementary materials (stacks.iop.org/MSMSE/22/055005/mmedia).

4.4. 3D NW growth

We are now ready to simulate the VLS growth of Ge NWs in the 3D phase field model. The initial condition is the equilibrated structure for the Ge–Au system containing a liquid

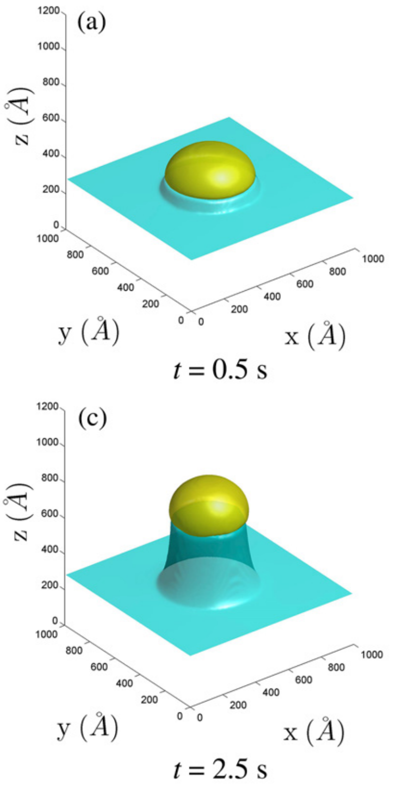

Figure 4. Simulation snapshots taken at different time. The initial condition is the equilibrated configuration shown in figure 3(*b*).

droplet at the Ge ⟨1 1 1⟩ substrate, shown in figure 3(*b*). The chemical potentials are set to $\mu_{\mathrm{V}} = 0.0269\,\mathrm{eV/atom} = 2.60\,\mathrm{kJ/mol}^{-1}$[7], $\mu_{\mathrm{S}} = 0$, with μ_{L} automatically adjusted to conserve Ω_{L}. Other simulation parameters are the same as those in section 4.3.

Figure 4 shows a series of snapshots at different time of the simulation. As the NW grows vertically, its diameter reduces from the initial spread of the catalyst droplet, before entering a steady state at which the top diameter remains constant. The side-wall facets are also observed and three side walls have a rougher morphology than the other three side walls. Figure 5 compares the side view of the NW predicted by this simulation with the TEM image of a real NW. In addition, the shape of the VLS triple junction is similar to TEM observations in the literature [24], especially the observation that the liquid–solid interface is not flat. More comparisons between simulation and experimental images are given figure S3 and figure S4 in Supplementary Materials (stacks.iop.org/MSMSE/22/055005/mmedia).

Figure 6(*a*) plots the height of the NW as a function of time at different chemical potential values μ_{V} for the same volume of the liquid droplet. At the beginning, all the curves overlap with each other. After about 2 s, the simulated NW growth behavior becomes different for

---

[7] The chemical potential μ_{V} of Ge in the vapor phase under experimental conditions is about $100\,\mathrm{kJ\,mol}^{-1}$, as estimated in section 5 of the Supplementary Materials. However, much of this chemical potential may be lost in the diffusion over gas phase and chemical decomposition at the liquid surface, which are not explicitly accounted for in our phase field model.

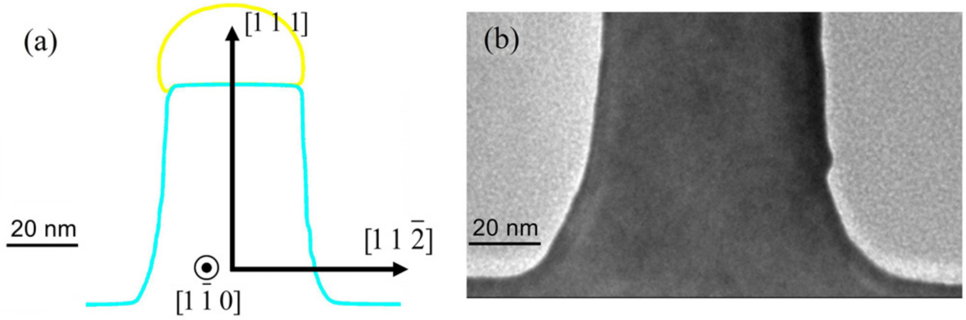

Figure 5. Side view of the NW base with the spherical droplet on its top from (*a*) the phase field simulation is compared to (*b*) the TEM image showing the NW base (courtesy of Yanying Li, Stanford University).

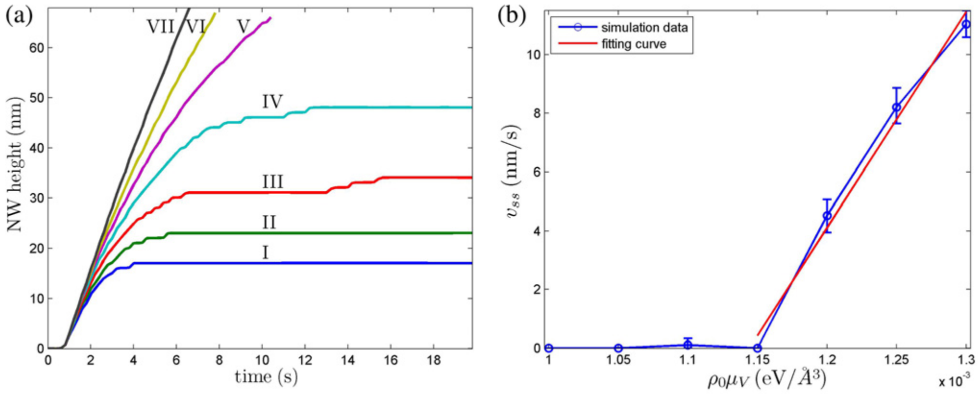

Figure 6. (*a*) NW height as a function of time at different vapor chemical potential for $D_{\mathrm{ss}} \approx 30\,\mathrm{nm}$. I: $\rho_0\mu_{\mathrm{V}} = 10 \times 10^{-4}\,\mathrm{eV/Å^3}$; II: $\rho_0\mu_{\mathrm{V}} = 10.5 \times 10^{-4}\,\mathrm{eV/Å^3}$; III: $\rho_0\mu_{\mathrm{V}} = 11 \times 10^{-4}\,\mathrm{eV/Å^3}$; IV: $\rho_0\mu_{\mathrm{V}} = 11.5 \times 10^{-4}\,\mathrm{eV/Å^3}$; V: $\rho_0\mu_{\mathrm{V}} = 12 \times 10^{-4}\,\mathrm{eV/Å^3}$; VI: $\rho_0\mu_{\mathrm{V}} = 12.5 \times 10^{-4}\,\mathrm{eV/Å^3}$; and VII: $\rho_0\mu_{\mathrm{V}} = 13 \times 10^{-4}\,\mathrm{eV/Å^3}$. (*b*) Steady-state NW growth velocity as a function of $\rho_0\mu_{\mathrm{V}}$ for $D_{\mathrm{ss}} \approx 30\,\mathrm{nm}$.

different chemical potential values μ_{V}. For sufficiently large μ_{V} ($\rho_0\,\mu_{\mathrm{V}} > 11.5 \times 10^{-4}\,\mathrm{eV/Å^3}$, i.e. $\mu_{\mathrm{V}} > 2.48\,\mathrm{kJ\,mol^{-1}}$), the NW eventually enters a steady-state growth regime with a constant growth rate v_{ss}. The top diameter of these NWs in steady-state growth is $D_{\mathrm{ss}} \approx 30\,\mathrm{nm}$. For smaller chemical potential μ_{V}, the NW growth stops before entering the steady state. This is because the free energy cost to create extra NW side walls (solid–vapor interface) is greater than the free energy reduction provided by transferring Ge from the liquid droplet to the solid. The effect of side wall surface energy effective reduces the chemical potential driving force by an amount proportional to σ_{SV}/D, where D is the NW top diameter. The NW top diameter D is an important factor that determines the chemical potential of the solid. Because D decreases during the early stage of growth, the NW may be able to grow to a certain height until D becomes small enough to terminate growth. In realty, the NW growth termination could be affected by other factors such as the angles of the sidewalls [25]. However, discussion about these factors is beyond the scope of this paper.

Figure 6(*b*) plots the steady-state NW growth velocity $v_{\rm ss}$ as a function of chemical potential $\mu_{\rm V}$ for a given catalyst size. $v_{\rm ss}$ is linear with $\mu_{\rm V}$ all the way until $v_{\rm ss}$ goes to zero. The linear dependence of steady-stage growth rate on the Ge chemical potential in the vapor phase (which is proportional to vapor pressure) is consistent with previous theoretical models [26, 27]. The simulation data are also fitted to the following equation, shown as the straight line in figure 6(*b*),

$$v_{\rm ss} = \alpha\, K_0^{\rm GL} \left[(\mu_{\rm V} - \mu_{\rm S})\, \rho_0 - \frac{\beta\, \sigma_{\rm SV}}{D_{\rm ss}} \right], \tag{37}$$

where $D_{\rm ss} = 30\,{\rm nm}$, $K_0^{\rm GL} = 10^4\,{\rm Å}^3/({\rm eV}\cdot{\rm s})$ and $\sigma_{\rm SV} = 0.0688\,{\rm eV/Å}^2$ is the average solid–vapor interface energy of the side wall of Ge NW growing along $\langle 1\,1\,1\rangle$ orientation, calculated from a separate simulation (as shown in section 6 of the Supplementary Materials, stacks.iop.org/MSMSE/22/055005/mmedia). $\alpha = 7\,{\rm nm}$ and $\beta = 4.7$ are empirical fitting parameters. Equation (37) describes the Gibbs–Thomson effect [6], in which thinner NWs can be in equilibrium with its vapor at a higher chemical potential. The NW growth velocity is proportional to the excess Ge chemical potential in the vapor phase, after the Gibbs–Thomson term (the second term in the square bracket) has been subtracted off.

5. Conclusion

We present a three dimensional multi-phase field model for NW growth by the VLS mechanism. The energetic parameters of the model are chosen to reproduce the experimental interface energies, while the kinetic coefficient $K_0^{\rm GL}$ is chosen to match the order of magnitude of the NW growth rate observed in experiments. The solid–vapor interface kinetic coefficients $K_{\rm SV}^{\rm GL}$ is set to be about three orders of magnitude lower than $K_0^{\rm GL}$, to reduce side-wall deposition. A diffusion term is included in the equation of motion to allow relaxation of the interface shape without changing the volume of any phases. The chemical potentials of the vapor and solid phases are specified as inputs, while the chemical potential of the liquid phase is automatically adjusted to conserve the volume of the liquid phase.

The phase field model passes several benchmark tests, including the Young's angle at the three phase junction and the faceted shape of nano-particle due to surface-energy anisotropy. Simulations with a chemical potential difference between the vapor and solid phase shows that for sufficiently high vapor chemical potential the growth eventually enters a steady state, but the growth can stop if the vapor chemical potential is not high enough. The phase field model presented here operates on the same length and time scale as experiments, and has the potential to help us understand NW growth anomalies such as kinking observed in experiments.

Acknowledgments

The authors thank Yanying Li and Dr Ann F Marshall for providing the TEM images. This work is supported by the National Science Foundation under grant No 1206511. SR acknowledges the support by Basic Science Research Program through the National Research Foundation of Korea (NRF) funded by the Ministry of Science, ICT & Future Planning (2013R1A1A010091).

References

[1] Law M, Goldberger J and Yang P 2004 Semiconductor nanowires and nanotubes *Annu. Rev. Mater. Res.* **34** 83–122

[2] Peng K-Q and Lee S-T 2011 Silicon nanowires for photovoltaic solar energy conversion *Adv. Mater.* **23** 198–215

[3] Schmidt V, Wittemann J V, Senz S and Gösele U 2009 Silicon nanowires: a review on aspects of their growth and their electrical properties *Adv. Mater.* **21** 2681–702

[4] Hannon J B, Kodambaka S, Ross F M and Tromp R M 2006 The influence of the surface migration of gold on the growth of silicon nanowires *Nature* **440** 69–71

[5] Dayeh S A, Wang J, Li N, Huang J Y, Gin A V and Picraux S T 2011 Growth, defect formation, and morphology control of germanium–silicon semiconductor nanowire heterostructures *Nano Lett.* **11** 4200–6

[6] Givargizov E I 1975 Fundamental aspects of VLS growth *J. Crystal Growth* **31** 20–30

[7] Kodambaka S, Tersoff J, Reuter M C and Ross F M 2007 Germanium nanowire growth below the eutectic temperature *Science* **316** 729–32

[8] Westwater J, Gosain D P, Tomiya S, Usui S and Ruda H 1997 Growth of silicon nanowires via gold/silane vapor–liquid–solid reaction *J. Vacuum Sci. Technol.* B **15** 554–7

[9] Ryu S and Cai W 2011 Molecular dynamics simulations of gold-catalyzed growth of silicon bulk crystals and nanowires *J. Mater. Res.* **26** 2199–206

[10] Wang H, Zepeda-Ruiz L A, Gilmerand G H and Upmanyu M 2013 Atomistics of vapour–liquid–solid nanowire growth *Nature Commun.* **4** 1956

[11] Bulatov V and Cai W 2006 Phase field method *Computer Simulations of Dislocations* (Oxford: Oxford University Press) chapter 11

[12] Schwarz K W and Tersoff J 2009 From droplets to nanowires: dynamics of vapor–liquid–solid growth *Phys. Rev. Lett.* **102** 206101

[13] Schwallbach E J 2011 Theoretical and computational approaches to vapor–liquid–solid nanowire growth *PhD Thesis* Northwestern University

[14] Wang N 2011 Phase-field studies of materials interfaces *PhD Thesis* Northeastern University

[15] Folch R and Plapp M 2003 Towards a quantitative phase-field model of two-phase solidification *Phys. Rev.* E **68** 010602

[16] Steinbach I and Pezzolla F 1999 A generalized field method for multiphase transformations using interface fields *Physica* D **134** 385–93

[17] Qin R S and Bhadeshia H K D H 2009 Phase-field model study of the effect of interface anisotropy on the crystal morphological evolution of cubic metals *Acta Mater.* **57** 2210–6

[18] Nadich Y V, Perevertailo V M and Obushchak L P 1975 Surface properties of binary melts, formed by gold with germanium and silicon *Zh. Fiz. Khim.* **49** 1554–6

[19] Jaccodine R J 1963 Surface energy of germanium and silicon *J. Electrochem. Soc.* **110** 524–7

[20] Eaglesham D J, White A E, Feldman L C, Moriya N and Jacobson D C 1993 Equilibrium shape of Si *Phys. Rev. Lett.* **70** 1643–6

[21] Adhikari H, Marshall A F, Goldthorpe I A, Chidsey C E D and McIntyre P C 2007 Metastability of Au–Ge liquid nanocatalysts: Ge vapor–liquid–solid nanowire growth far below the bulk eutectic temperature *ACS Nano* **1** 415–22

[22] Stekolnikov A A and Bechstedt F 2005 Shape of free and constrained group-IV crystallites: influence of surface energies *Phys. Rev.* B **72** 125326

[23] Ringe E, Van Duyne R P and Marks L D 2011 Wulff construction for alloy nanoparticles *Nano Lett.* **11** 3399–403

[24] Gamalski A D, Ducati C and Hofmann S 2011 Cyclic supersaturation and triple phase boundary dynamics in germanium nanowire growth *J. Phys. Chem.* C **115** 4413

[25] Schwarz K W and Tersoff J 2011 Elementary processes in nanowire growth *Nano Lett.* **11** 316–20

[26] Schmidt V, Senz S and Gösele U 2007 Diameter dependence of the growth velocity of silicon nanowires synthesized via the vapor–liquid–solid mechanism *Phys. Rev.* B **75** 045335

[27] Jagannathan H, Deal M, Nishi Y, Woodruff J, Chidsey C and McIntyre P C 2006 Nature of germanium nanowire heteroepitaxy on silicon substrates *J. Appl. Phys.* **100** 024318